



Research Paper

Clay rich river sediments calcined into precursors for alkali activated materials

Lea Žibret^a, Wolfgang Wisniewski^a, Barbara Horvat^a, Mojca Božič^b, Boštjan Gregorc^b, Vilma Ducman^{a,*}^a Slovenian National Building and Civil Engineering Institute (ZAG), Dimičeva 12, Ljubljana 1000, Slovenia^b Hydropower Plant Dravske Elektrarne Maribor (DEM), Obrežna ulica 170, Maribor 2000, Slovenia

ARTICLE INFO

Keywords:

River sediment
 Calcination
 Alkali activated materials
 Ladle slag
 Fly ash
 Mechanical strength

ABSTRACT

Alkali activated materials (AAMs), a potential alternative to cement-based products or ceramics, can incorporate large amounts of currently landfilled aluminosilicate rich materials such as calcined clay-rich river sediments collected at hydropower plant dams. Untreated fresh sediment and untreated aged sediment intended to serve as AAM precursors were calcined to increase their amorphous content, then activated by Na or K-based silicate or hydroxide solutions and cured at 60 °C for three days.

Up to 30 mass % (ma%) of fly ash (FA) or ladle slag (LS) increased the mechanical performance. The phase composition and microstructure are analyzed using X-ray diffraction, fourier-transform infrared spectroscopy, scanning electron microscopy, energy dispersive X-ray spectroscopy and mercury intrusion porosimetry to gain further insight into how the additives influence the final properties of the resulting AAMs. The main crystalline components of the prepared AAMs are quartz, illite/muscovite and feldspar. The amorphous content reaches up to 52.5 ma% in the Na-activated AAMs and up to 48.8 ma% in K-activated AAMs. The acquired results confirm the suitability of the investigated sediments as sole precursors for AAMs. The mechanical properties of the AAMs can be improved by adding FA and/or LS.

1. Introduction

One of the promising low carbon-footprint inorganic polymeric material classes requiring a moderate energy use in the building sector are the alkali activated materials (AAMs) (Khale and Chaudhary, 2007; Provis et al., 2015; Provis, 2018). They can be produced by the alkali activation of mostly amorphous aluminosilicates (Davidovits, 2017). Compared to ordinary Portland cement (OPC), their production can reduce the CO₂ release by up to 64% (McLellan et al., 2011) while showing a performance sufficient for a wide range of applications in civil engineering (Nawaz et al., 2020). Even if the energy used for producing alkaline activators and elevated-temperature curing is taken into account, the CO₂ emission is still 9% lower than for OPC binders (Turner and Collins, 2013).

Clay minerals are available worldwide and seem to be a promising aluminosilicate choice for the production of AAMs (Khalifa et al., 2020). A commonly used precursor is metakaolin (Sarkar et al., 2015; Sabbatini et al., 2017; Koutník et al., 2020; Traven et al., 2021), i.e. calcined

kaolin, which is a valuable material of limited availability. Lower quality raw materials such as kaolinite claystone (Hájková, 2018), argillite rock (Dupuy et al., 2018), shales with a variety of clay minerals (El-Habaak et al., 2018), sedimentary clays obtained from dams containing kaolinite, illite, quartz and calcite (Mostefa et al., 2018), clay washing residues (Sgarlata et al., 2021) or gravel wash mud (Thapa et al., 2018) have also been shown to be suitable AAM precursors after calcination. AAMs of low quality can also be successfully formed from un-calcined montmorillonite or illite clay (Marsh et al., 2018).

AAM mixtures can be made from various industrial by-products like fly ash (FA) and ground granulated blast furnace slag (Huseien et al., 2019), ladle slag (LS) (Bignozzi et al., 2013), red mud (Kumar and Kumar, 2013), paper sludge (Yan and Sagoe-Crentsil, 2012), mine tailings (Obenaus-Emler et al., 2020), municipal solid waste incineration ash (Wongsa et al., 2017) and/or waste ceramics (Huseien et al., 2019) etc., providing a great potential to prevent a massive landfilling of harmful waste materials (Bernal et al., 2016) and to save space in the landfills (Pavlin et al., 2022). Another advantage of AAMs is their

* Corresponding author.

E-mail address: vilma.ducman@zag.si (V. Ducman).<https://doi.org/10.1016/j.clay.2023.106848>

Received 16 November 2022; Received in revised form 21 January 2023; Accepted 29 January 2023

Available online 15 February 2023

0169-1317/© 2023 The Authors. Published by Elsevier B.V. This is an open access article under the CC BY license (<http://creativecommons.org/licenses/by/4.0/>).

potential to immobilize toxic metals such as Co, Cu, Pb, Cd, Ni, Zn, Pd, As, Ra and U in the aluminosilicate network (ASN) consisting of Si and Al tetrahedra connected with O-bridges. The mobility of toxic elements is lowered by the precipitation of metal hydroxides, ion substitution or physical encapsulation in the ASN (Guo et al., 2014; Boldrini et al., 2021).

Large quantities of clay-rich sediments suitable as AAM precursors are accumulating at hydropower plant dams worldwide (Ferone et al., 2015). In this study, carbonate-rich illite clay sediments from the Dravske elektrarne Maribor hydropower plants in Slovenia are tested for their suitability as AAM precursors. Although these sediments show elevated levels of Zn, Pb and Cd, they can be used in clay based construction materials without any pretreatment (Ducman et al., 2022). Materials suitable as a precursor in alkali activated synthesis for alternative construction industry products should show a high reactivity in alkali media, i.e. a significant dissolution of Si and Al which are the main building blocks in the ASN (Škvára, 2007). The reactivity of clay rich sediments can be increased by calcination (D'Elia et al., 2018) (D'Elia et al., 2020).

The work presented here concerns untreated fresh sediment (FS₀) and untreated aged sediment (AS₀) as well as their respective counterparts calcined fresh sediment (FS) and calcined aged sediment (AS). The solubility of the FS and AS in alkaline solutions was tested to evaluate their suitability for alkali activation. AAMs were prepared using calcined sediments, FA and LS activated with Na-based or K-based alkali activators. The prepared mixtures were evaluated by measuring their compressive strength. Selected AAMs were also analyzed using Fourier-transform infrared spectroscopy (FTIR), X-ray diffraction (XRD), mercury intrusion porosimetry (MIP), scanning electron microscopy (SEM) and energy dispersive X-ray spectroscopy (EDXS) to gain further insight into the alkali activation process. The increasing use of renewable energy resources means increasing amounts of clay rich river sediments accumulating behind hydropower dams which calls for new strategies for their long-term management. The aim of this study is to evaluate their suitability as AAM precursors in the building sector.

2. Experimental methods

Four raw materials were used to prepare precursors for AAMs: FS₀ deposited for less than one year, AS₀ deposited for 10 years, coal-combustion FA from a local thermal power plant (Traven et al., 2021) and LS from the desulfurization at the second stage of steel refining (Češnovar et al., 2019). The provenance of the Drava sediments is strongly related to the region of Hohe Tauern (Schmid et al., 2013) as well as to the local lithological units (Šoster et al., 2017). The Drava river shows an additional anthropogenic geochemical association related to historical Zn and Pb smelting in the upstream area (Šajn et al., 2011). While the FA was used as received, the LS was ground to a grain size below 125 μm using a vibrating disk mill Labor-Scheibenschwingmühle TS.250 (Siebtechnik GmbH, Mülheim an der Ruhr, Germany). The FS₀ and AS₀ were also ground to a grain size below 90 μm and calcined in a HLF 100 laboratory furnace (Protherm) by heating them to 900 °C using a heating rate of 5 °C/min and holding them for 20 min at 900 °C before they were removed from the furnace and allowed to rapidly cool under room conditions.

The dissolution of Si and Al from the precursors was determined using a Varian 715-ES ICP Optical Emission Spectrometer (Agilent HP). The samples were sieved to a grain size below 63 μm and 1.0 (±0.0001) g were mixed with 40 mL of 10 M NaOH or 10 M KOH for 24 h under continuous stirring (Panagiotopoulou et al., 2007). 65% HNO₃ was added to lower the pH <2 before the analysis.

The loss on ignition (LOI) of the precursors, dried to a constant mass in an IR moisture analyzer (Mettler Toledo, HE73) at 105 °C, was determined by respectively heating ca. 3–4 g at 550 °C with a holding time of 2 h. After cooling, the same samples were heated at 950 °C and held for another 2 h. The resulting ignited samples were mixed with

Fluxana (Li-tetraborate and Li-metaborat mixed in a mass ratio of 1:1) at a ratio of 1:10 and melted into discs. LiBr_(l) (50 mL H₂O and 7.5 g of LiBr_(s) from Sigma Aldrich) was added to the mixture to avoid gluing the melt to the Pt crucible. The chemical compositions were then determined using a ARL PERFORM[®]X sequential X-ray fluorescence (XRF) Spectrometer (Thermo Fisher Scientific Inc., Ecublens, Switzerland) using the UniQuant 5 software (Thermo Fisher Scientific Inc., Waltham, MA, USA).

The densities of the AAM precursors FS₀ and AS₀ were determined according to EN 1097-7 (SIST EN 1097-7, 2008) using a pycnometer after drying them in a laboratory oven for approximately 20 h at 105 °C.

The particle size distribution (PSD) of FS₀, AS₀, FS, AS, LS and FA was measured by laser diffraction granulometry using a Sync+Turbo-Sync laser grain size analyzer (Microtrack MRB) in the dry dispersion measurement mode. The FA was sieved to a grain size below 0.5 mm for this measurement.

Nitrogen adsorption measurements of FS, AS, LS and FA were performed by Micromeritics ASAP-2020 analyzer (Micromeritics, Norcross, GA, USA). The samples were sieved to a grain size below 63 μm and dried in a laboratory oven for approximately 20 h at 105 °C. The mass of the analyzed samples was approximately 1.5 g. The total specific surface area was determined using the Brunauer–Emmet–Teller (BET) method.

Alkali activators were prepared by mixing the Na-water glass (Geosil 34417: 27.5 mass % (ma%) SiO₂ and 16.9 ma% Na₂O) with 10 M NaOH or the K-water glass (Betol K 5020 T: 30.1 ma% SiO₂ and 18.5 ma% K₂O) with 10 M KOH. The SiO₂ : Na₂O or SiO₂ : K₂O mass ratio of both used water glasses was 1.63. However, the molar ratio of SiO₂ : Na₂O in Na-water glass was 1.68, while that in the K-based water glass of SiO₂ : K₂O was 2.55. Consequently, Na- and K-based AAMs were described separately. The AAM batches were prepared according to Table 1 using FS or AS as well as 10, 20 or 30 ma% replacements with FA or LS.

Three sample prisms of 20 × 20 × 80 mm³ were prepared for each AAM batch in Table 1 using silicone moulds. After three days of curing in a temperature and humidity controllable chamber KK 240 SMART PRO (POL-EKO-APARATURA SP.J., Poland) at 60 °C and variable relative humidities (R.H. = 30–60%; 1st day 60%, 2nd day 50%, 3rd day 30%) the bending and compressive strengths were measured using a ToniPRAX (ToniTechnik, Berlin, Germany) at a force rate of 0.05 kN/s. The samples were stored in closed plastic bags for approximately one year before their microstructural investigation.

XRD was performed using a PANalytical Empyrean X-ray diffractometer with CuKα radiation (wavelength CuKα₁ 1.54 Å). The precursors as prepared for mixing and the AAMs ground to a grain size below 63 μm were manually back-loaded into a cylindrical sample holder (diameter of 27 mm) to mitigate the preferred orientation effect for XRD data collection. Each sample was measured from 2θ = 4° to 70° while being spun. Instrument configuration: soller slits 0.04 rad; incident beam mask 15 mm; slit 2°; step size 0.0131°; counting time 198.645 s. The X-ray tube was operated at 45 kV and 40 mA. Rietveld refinements were performed using the PANalytical X'Pert High Score Plus diffraction software v. 4.8. The amorphous phase was analyzed using the external standard method (Madsen et al., 2011) with Al₂O₃ powder (NIST676a) as the reference material.

FTIR was performed using a PerkinElmer Spectrum Two in attenuated total reflection mode (Universal ATR with diamond/ZnSe crystal) in the range from 380 cm⁻¹ to 4000 cm⁻¹ with a resolution of 4 cm⁻¹ on the prepared precursors FS₀, FS, FA, LS, and the AAMs ground to a grains size below 125 μm. Peak minima were determined using the PerkinElmer Spectrum Quant software. The low water content of the samples enabled to determine the band location and area of Si-O-Si asymmetric stretching vibrational modes (Lucas et al., 2011).

The pore distribution of the produced AAMs was measured using MIP. Small representative fragments were dried to a constant mass in an oven (Binder) at 70 °C under laboratory atmosphere and analyzed using a Micromeritics®Autopore IV 9500 (Micromeritics, Norcross, GA, USA).

AAMs were cast in acrylic resin and dry polished. Prepared uncoated

Table 1

Prepared AAM batches (g). Abbreviations: AS - calcined aged sediment, FS - calcined fresh sediment, FA – fly ash, LS – ladle slag.

sample designation	AS	FS	FA	LS	Geosil 34417	Betol K5020 T	10 M NaOH	10 M KOH
pure AS (Na)	100	–	–	–	55	–	17.5	–
AS-10FA	90	–	10	–	55	–	17.5	–
AS-20FA (Na)	80	–	20	–	55	–	17.5	–
AS-30FA (Na)	70	–	30	–	55	–	17.5	–
AS-10LS (Na)	90	–	–	10	55	–	17.5	–
AS-20LS (Na)	80	–	–	20	55	–	17.5	–
AS-30LS (Na)	70	–	–	30	55	–	17.5	–
pure AS (K)	100	–	–	–	–	55	–	17.5
AS-10FA (K)	90	–	10	–	–	55	–	17.5
AS-20FA (K)	80	–	20	–	–	55	–	17.5
AS-30FA (K)	70	–	30	–	–	55	–	17.5
AS-10LS (K)	90	–	–	10	–	55	–	17.5
AS-20LS (K)	80	–	–	20	–	55	–	17.5
AS-30LS (K)	70	–	–	30	–	55	–	17.5
pure FS (Na)	–	100	–	–	55	–	17.5	–
FS-20FA (Na)	–	80	20	–	55	–	17.5	–
FS-30FA (Na)	–	70	30	–	55	–	17.5	–
FS-10LS (Na)	–	90	–	10	55	–	17.5	–
FS-20LS (Na)	–	80	–	20	55	–	17.5	–
FS-30LS (Na)	–	70	–	30	55	–	17.5	–
pure FS (K)	–	100	–	–	–	55	–	17.5
FS-10FA (K)	–	90	10	–	–	55	–	17.5
FS-20FA (K)	–	80	20	–	–	55	–	17.5
FS-30FA (K)	–	70	30	–	–	55	–	17.5
FS-10LS (K)	–	90	–	10	–	55	–	17.5
FS-20LS (K)	–	80	–	20	–	55	–	17.5
FS-30LS (K)	–	70	–	30	–	55	–	17.5

polished cross-sections were examined using SEM and EDXS performed with a JEOL IT500 LV SEM equipped with an Ultim Max Detector (Oxford Instruments) operated in low vacuum mode with an accelerating voltage of 20 kV. EDXS was performed using the software Aztec 5.0 SP1 (Oxford Instruments Nanotechnology Tools Ltd).

3. Results and discussion

3.1. Characterization of calcined sediments

The chemical composition of the AAM precursors determined using XRF is stated in Table 2 along with the measured LOI and densities. The sediments show similar compositions except that ASo shows a higher relative concentration of SiO₂, as already identified in a previous study that showed ASo to contain about 5 ma% more crystalline SiO₂ than the FSo. Probably clay is washed from the sediment during the longer exposure to climatic conditions which increases the relative amount of e. g. quartz (Ducman et al., 2022). FA had a SiO₂ amount similar to FSo, but more Al₂O₃ and CaO. LS had the lowest contents of SiO₂, Al₂O₃, Na₂O and K₂O but contains the maximum amounts of CaO and MgO. The FA contains incompletely combusted cellulose (Horvat et al., 2022) and shows the lowest density while LS has a comparably high metal content (Česnovar et al., 2019) and shows the highest density (Table 2). As expected, calcination decreases the sediment densities.

The main percentiles from the PSD of the precursors are stated in Table 2; the detailed distributions are provided in Supplement 1. FSo and ASo were ground to a grain size below 90 μm because, as deposited, these sediments only show a grain size below 200 μm (Ducman et al., 2022). LS shows a slightly bimodal PSD and the FA shows a right-shifted curve which means it contains coarser particles than the other used precursors. SEM analysis of the calcined AS and FS showed that they mainly contain angular/irregular and flaky particles (used terminology after Nouri and Sola, 2018), while FA mainly contains spherical/rounded grains, micrographs are provided as Supplement 2. Some larger FA particles probably broke and hence show edges. LS contains angular grains as well as some rounded grains. The amorphous content in ASo was 27 ma% but increased to 32 ma% during calcination. The amorphous content in FSo was 34 ma% and increased to 38 ma% during

Table 2

Chemical composition of the AAM precursors (ignited at 950 °C) measured by XRF, the values of FA are transferred from (Traven et al., 2021) while those of LS originate from (Česnovar et al., 2019). The LOI, density, and main percentiles of the PSD are also stated. Abbreviations: ASo - untreated aged sediment, AS - calcined aged sediment, FSo - untreated fresh sediment, FS - calcined fresh sediment, FA – fly ash, LS – ladle slag, LOI – loss on ignition, PSD – particle size distribution.

	ASo	AS	FSo	FS	FA	LS
SiO ₂ [ma%]	54.8	54.4	55.6	52.5	45.1	17.2
Al ₂ O ₃ [ma%]	18.4	18.9	17.9	19.1	23.1	6.5
Fe ₂ O ₃ [ma%]	6.7	6.6	6.3	6.7	10.7	5.9
CaO [ma%]	7.5	7.5	7.8	8.6	12.4	35.0
MgO [ma%]	6.0	6.2	5.9	6.3	2.8	29.2
Na ₂ O [ma%]	1.5	1.5	1.6	1.5	1.2	0.4
K ₂ O [ma%]	2.8	2.7	2.6	2.7	2.2	0.2
SO ₃ [ma%]	0.5	0.5	0.4	0.5	0.8	1.5
MnO [ma%]	0.1	0.1	0.1	0.1	0.3	0.8
P ₂ O ₅ [ma%]	0.2	0.2	0.2	0.2	0.4	0.1
TiO ₂ [ma%]	1.0	1.0	1.0	1.0	0.7	0.2
ZnO [ma%]	0.2	0.2	0.2	0.2	0.0	0.6
As ₂ O ₃ [ma%]	0.1	0.1	0.1	0.1	0.0	0.0
ZrO ₂ [ma%]	0.0	0.0	0.0	0.0	0.0	0.2
Cr ₂ O ₃ [ma%]	0.0	0.0	0.0	0.0	0.0	0.2
SrO [ma%]	0.0	0.0	0.0	0.0	0.0	0.1
BaO [ma%]	0.1	0.1	0.1	0.1	0.1	0.0
LOI 550 °C [ma%]	6.4	0.0	6.5	0.0	0.9	4.5
LOI 950 °C [ma%]	13.8	0.0	15.2	0.0	0.9	17.4
density [g/cm ³]	2.634	2.771	2.657	2.764	2.417	2.871
PSD d ₉₀ [μm]	65.2	67.1	68.5	69.0	151.5	90.1
PSD d ₅₀ [μm]	15.7	17.6	19.2	21.0	41.7	15.3
PSD d ₁₀ [μm]	1.8	1.3	1.8	1.4	3.5	0.8

calcination. FS and LS showed 38 ma% while showed FA 76 ma% amorphous phase. Detailed XRD results including the respective agreement indices and goodness of fit parameters of the refinement are provided as Supplement 3.

FTIR measurements performed on selected precursors are presented in Supplement 4. Water is indicated by asymmetric and symmetric stretching vibrations of the O–H group and bending vibration of H–O–H

in FTIR spectra (Razak et al., 2015). Water is hence detected in the FSO spectrum (minima around 3376 cm⁻¹ and 1634 cm⁻¹) but, as is to be expected, neither in the calcined sediment FS nor FA and LS which are waste materials from high-temperature processes.

Carbonates are indicated by asymmetric stretching vibrations and out-of-plane bending vibrations of CO₃²⁻ (Komnitsas et al., 2015; Khater and Abd el Gawaad, 2016). These vibrations respectively cause the broad peak with a minimum at 1442 cm⁻¹ and a prominent local minimum at 881 cm⁻¹ in FSo and are significantly less intense in the spectrum of FS. It only shows a residue of the broader peak (1415 cm⁻¹) because calcination at ≤900 °C failed to decompose the carbonates completely. Carbonates were also found in LS (minima at 1428 cm⁻¹ and at 874 cm⁻¹) where the narrow out-of-plane bending peak indicates the presence of crystalline carbonates besides amorphous carbonates.

Quartz (low/alpha) is indicated by the symmetrical stretching vibration of Si-O-Si bonds (Khater and Abd el Gawaad, 2016) and detected by the peak minima ranging from 793 cm⁻¹ to 798 cm⁻¹). The most prominent broad peak in the FA spectrum has a minimum at 992 cm⁻¹ for FA and at 988 cm⁻¹ for all other precursors and can be attributed to the asymmetric vibrations of Si-O-T (T = Si or Al) in the tetrahedral groups of silicates (Rovnaník et al., 2013; Gao et al., 2015; Messina et al., 2017).

Calcinating clay sediments significantly improves the solubility of Si and Al, independent of the clay mineral type (Werling et al., 2022). Dissolution results for the AAM precursors are presented in Table 3 and show that the 10 M NaOH solution only dissolved 134 mg/L of Si and 54 mg/L of Al from ASo and only 115 mg/L of Si and 46 mg/L of Al from FSo. The 10 M KOH solution only dissolved 105 mg/L of Si and 36 mg/L of Al from ASo and only 94 mg/L of Si and 34 mg/L of Al from FSo. Table 3 confirms a respectively high solubility of Si and Al from both calcined sediments but the largest total amount of Si and Al are dissolved from FA due to their high absolute content and the highest amorphous phase content. Lower dissolution levels of LS compared to FA can be attributed to lower total content of Si and Al (Table 1, Table 3). All precursors generally showed a better solubility in NaOH than in KOH, which is in agreement with the literature (Panagiotopoulou et al., 2007).

3.2. Alkali activation of calcined sediments with a Na-based activator and performance improvement by adding FA or LS

Samples for mechanical testing using the mixtures of calcined FS and AS with 10 M NaOH were prepared as stated in Table 1. The measured bending and compressive strengths as well as the geometrical densities are presented in Fig. 1, the corresponding values are provided as Supplement 5. The AAMs based on the FS generally showed higher strengths and comparable or lower densities than those based on the AS, which contains a slightly higher amount of SiO₂, see Table 2. The compressive

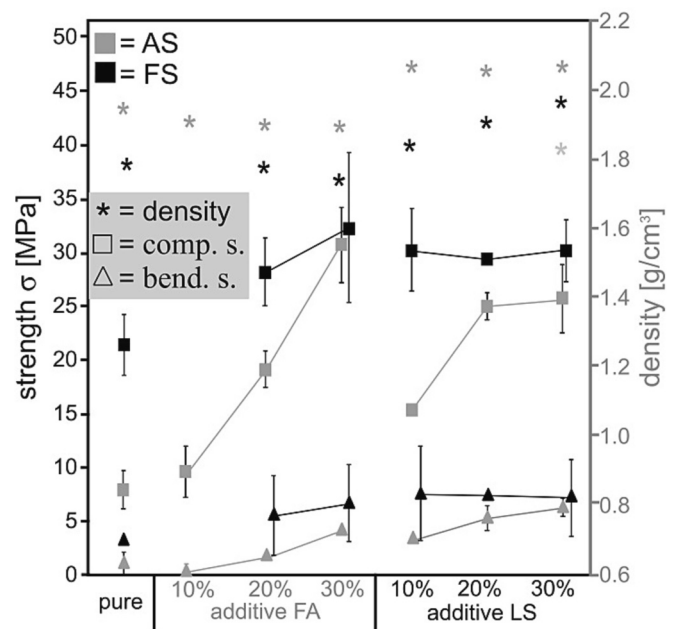


Fig. 1. Compressive and bending strengths of the Na-activator based AAMs as well as their geometrical density, measured after curing for three days. Abbreviations: AS - calcined aged sediment, FS - calcined fresh sediment, FA - fly ash, LS - ladle slag.

strength of the FS activated mixture reached 21.3 MPa, while the AS base mixture reached a compressive strength of 7.9 MPa. Up to 30 ma% FA or LS were added and improved the mechanical properties, as is discernible in Fig. 1; adding 30 ma% of FA or LS to FS increased the compressive strength up to 32.2 or 29.3 MPa, respectively, while the same additions to AS resulted in compressive strengths of respectively 30.7 and 25.6 MPa.

Mineralogical and microstructural investigations were performed on selected precursors and the FS-AAMs showing the highest strengths. XRD-patterns acquired from pure FS-AAMs and those with additions of 30 ma% FA or LS activated using Na-activator are presented in Fig. 2, the reflections with highest intensities of selected phases identified during subsequent evaluation are highlighted.

They are all similar at a first glance but some relative reflection intensities vary. One notable reflection at 2θ ≈ 6° has been attributed to the formation of zeolites during AAM synthesis (Provis et al., 2005). Na-salts are identified in the AAMs e.g. by the reflection at 2θ ≈ 24.2° (thermonatrite Na₂CO₃xH₂O) due to the surplus of activators which

Table 3

The amount of Si and Al dissolved from the analyzed precursors and non-calcined sediments in 10 M NaOH and 10 M KOH in [mg/L] and [mmol/L], compared by total Si and Al content in [mmol/L] (XRF results from Table 2) and BET specific surface area. Abbreviations: ASo - untreated aged sediment, AS - calcined aged sediment, FSo - untreated fresh sediment, FS - calcined fresh sediment, FA - fly ash, LS - ladle slag.

dissolution liquid	element	units	ASo	AS	FSo	FS	FA	LS
10 M NaOH	Si	mg/L	134.0	627.0	115.0	579.0	822.0	396.0
		mmol/L	4.8	22.3	4.1	20.6	29.3	14.1
	Al	mg/L	54.0	192.0	46.0	168.0	351.0	104.0
		mmol/L	2.0	7.1	1.7	6.2	13.0	3.9
10 M KOH	Si	mg/L	105.0	480.0	94.0	471.0	655.0	375.0
		mmol/L	3.7	17.1	3.3	16.8	23.3	13.3
	Al	mg/L	36.0	130.0	34.0	117.0	271.0	66.0
		mmol/L	1.3	4.8	1.3	4.3	10.0	2.5
total content (XRF)	Si	mmol/L	228.1	226.2	231.7	219.2	187.9	72.9
	Al	mmol/L	90.3	92.6	87.9	94.0	113.4	32.5
BET specific surface area		m ² /g	5.5	5.5	5.9	5.2	2.8	4.9

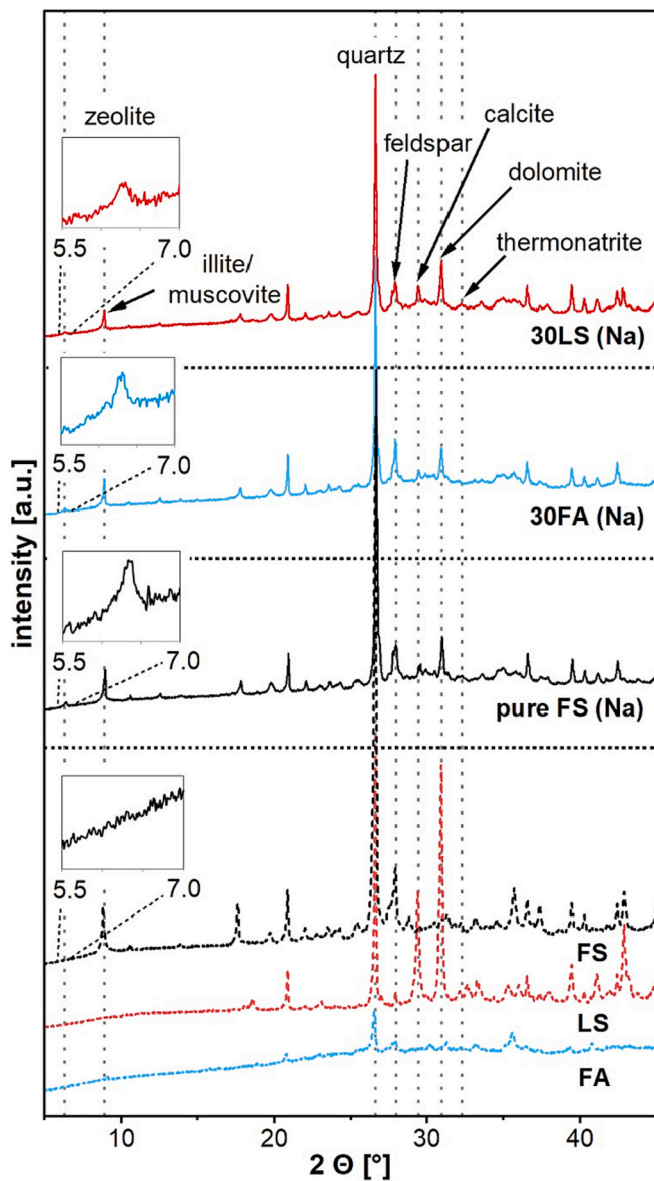


Fig. 2. XRD patterns of powdered precursors and FS-AAMs prepared using the pure sediment or containing 30 ma% FA or LS and activated using Na-based solutions. The highest intensity reflections of subsequently identified phases are highlighted. The frames highlight the area around 6° . Abbreviations: FS - calcined fresh sediment, FA - fly ash, LS - ladle slag.

caused efflorescence, a common phenomenon in silica-dominant systems with a high concentration alkaline activators (Xiao et al., 2020).

A detailed Rietveld refinement was performed on XRD-patterns acquired from powders of the respective AAMs. The main crystalline components of the prepared AAMs are quartz, illite/muscovite and feldspar. Calcite and dolomite respectively occur in amounts below 1.8 and 6.0 ma%. Na_2CO_3 was detected in the Na-based AAMs but does not occur in any of the precursors, hence it can be assumed to have formed after curing for 72 h and aging for 1 year. Trace amounts of respectively <1.0 ma% MnCr_2O_4 , brucite, coesite, mullite, MgFeO_4 , gehlenite and/or larnite were indicated in the precursors but not in the AAMs. The amorphous content in the Na-activator AAMs ranges from 41 to 53 ma% and is hence always higher than that of the main precursor FS (38 ma%). While the elevated amorphous content in FA containing AAMs is not surprising, the amorphous content in LS containing AAMs ranges from 43 to 53 ma%, i.e. is always higher than in either precursor. This certainly results from the residue of the added water glass but can also

result from the formation of an amorphous gel during the alkali activation process. The complete results are provided as Supplement 3.

The FTIR spectra of cured AAMs and the respectively used precursors are shown in Fig. 3.

All AAMs contained water (minima between 1100 cm^{-1} and 1200 cm^{-1} and between 1645 cm^{-1} and 1652 cm^{-1}) as well as quartz from the precursors (minima between 795 cm^{-1} and 798 cm^{-1}).

Although LS was the only precursor with an appreciable amount of amorphous and crystalline carbonates, all AAMs contained carbonates (minima between 1393 cm^{-1} and 1417 cm^{-1} and peaks/shoulders from 868 cm^{-1} to 882 cm^{-1}), implying that the samples carbonated during curing, probably due to the excess of 1st and 2nd group elements in the periodic table. AAMs prepared using Na-water glass and NaOH show an additional peak with a minimum of about 1485 cm^{-1} regardless of the precursors. It is attributed to the asymmetric stretching of C=O in Na-carbonates (thermonatrite) (Mabrouh et al., 2020) and is in agreement with the XRD results presented in Fig. 2 and Supplement 3.

Most importantly, all AAM spectra in Fig. 3 show a peak indicating

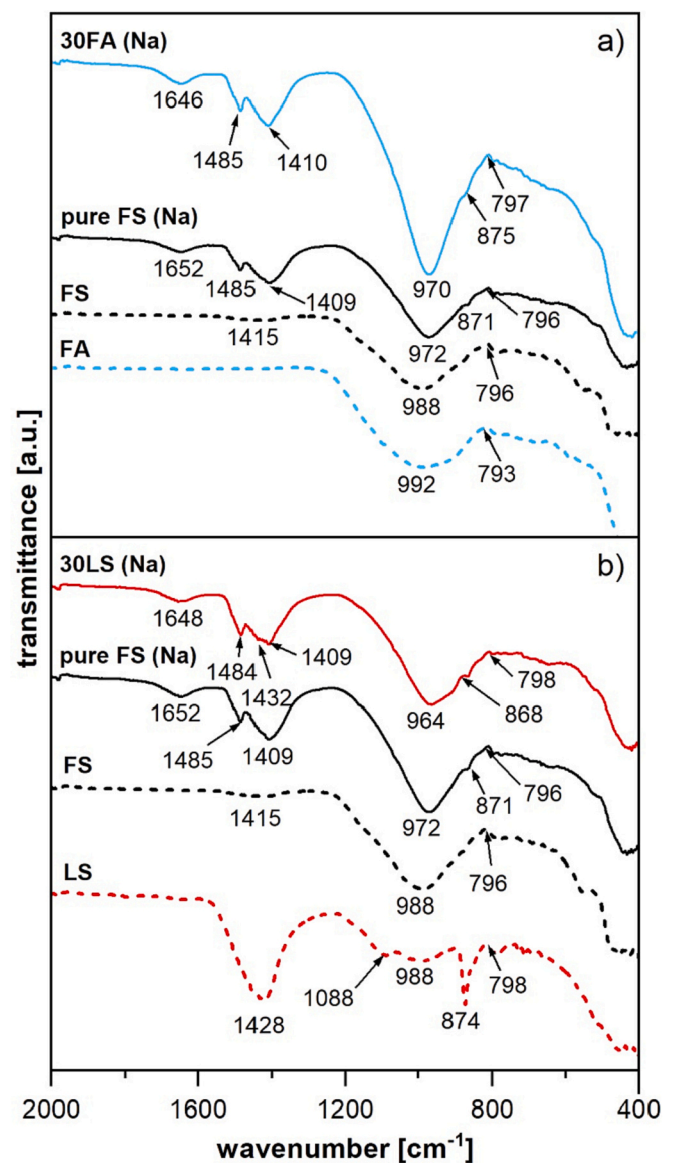


Fig. 3. FTIR spectra of the powdered precursors and FS-AAMs prepared using the pure sediment or containing 30 ma% a) FA or b) LS and activated using Na-based solutions. Abbreviations: FS - calcined fresh sediment, FA - fly ash, LS - ladle slag.

Si-O-T asymmetric vibrations with minima between 964 cm^{-1} and 979 cm^{-1} , i.e. shifted to lower wavenumbers than the same peaks in the precursors, see Supplement 4 (988 cm^{-1} and 992 cm^{-1}), implying that the Si/Al ratio in the ASN increased in favor of Si (Hajimohammadi et al., 2010). This could be partially due to the better dissolution of Si than Al in the alkali media, see Table 3, but also due to the presence of Si in the Na-water glass which got incorporated into the ASN.

The porosity and PSD of the investigated mixtures determined by MIP are presented in Fig. 4 and Table 4.

The pure Na-activated AAM had a total porosity of 20.78% with a bi-modal pore size distribution showing a larger peak between 0.1 and 2.0 μm . A bi-modal porosity distribution is also observed after adding 30 ma % FA but the pore sizes above 0.5 μm shift to higher values. On the other hand, pores in AAMs containing 30 ma% LS show a unimodal distribution with most pores showing sizes from 0.1 to 2.0 μm in diameter, i.e. a shift towards smaller pores compared to the pure FS AAM. Hence adding FA increased the porosity while adding LS reduced it, as also indicated by the measured densities in Table 4. Despite the increased porosity in the Na-activated AAMs containing FA, their compressive strengths are also higher, see Fig. 1 and Supplement 5. Adding LS decreased the porosity of the AAMs but the compressive strengths presented in Fig. 1 and Supplement 5 remained constant.

The pores with diameters of around 0.01 μm indicated in Fig. 4 can be attributed to the ASN/gel which is characteristic for alkali activation synthesis (Chen et al., 2022). However, all cementitious OPC and AAM based binders include a sub-micron porosity with a complex geometry (Promentilla et al., 2009), which is challenging to characterize (Provis et al., 2012). In AAMs, highly interconnected gel interstices (nano pores) range from 2 to 100 nm (Lee et al., 2014; Chen et al., 2022), while pores with diameters of 100 nm to 10 μm (meso and micro pores) are attributed to isolated vacancies between particles, fillers and defects (Chen et al., 2022). Gel pores are too small to initiate cracking when loaded (Kendall et al., 1983), while meso and micro pores are usually very isolated and mainly connected by the finer pore network of the gel (Chen et al., 2022). This might partially explain why the compressive strength did not decrease when the porosity increased upon adding FA. Macro pores with diameters $>10\text{ }\mu\text{m}$ are generally attributed to air bubbles (Chen et al., 2022). SEM analyses of the morphology and distribution of macro pores in the AAMs revealed the presence of spherical macro pores (diameters from 10 to around 100 μm) and cracks, SEM micrographs and EDXS element maps are provided as Supplement 6, Supplement 7 and

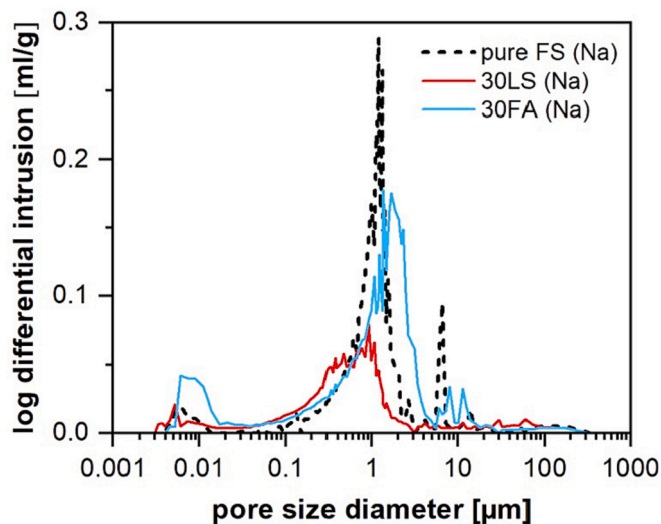


Fig. 4. Log differential intrusion vs. pore size of the powdered precursors and FS-AAMs prepared using the pure sediment or containing 30 ma% FA or LS and activated using Na-based solutions. Abbreviations: FS - calcined fresh sediment, FA - fly ash, LS - ladle slag.

Table 4

Results of the MIP analysis of Na-activated samples. Abbreviations: FS - calcined fresh sediment, FA - fly ash, LS - ladle slag.

sample	FS [ma %]	porosity [%]	average pore diameter [μm]	median pore diameter [μm]	bulk density [g/mL]	skeletal density [g/mL]
pure FS (Na)	–	20.78	0.11	1.11	1.98	2.50
FS-30FA (Na)	30	24.14	0.07	1.34	1.81	2.38
FS-30LS (Na)	30	14.25	0.06	0.56	2.09	2.44

Supplement 8. The spherical pores probably contain gas trapped during mixing and/or the chemical reaction with the alkali activators. The cracks (width around 1–2 μm) can be attributed to the drying shrinkage during AAM curing (Kuenzel et al., 2012) and their occurrence was similar in the pure FS AAM, see Supplements 6 a-c and 7 a, and 30 ma% FA containing AAM, see Supplements 6 d-f and 7 b. Spherical pores were cut by cracks, see Supplement 6 d and g. As MIP did not confirm the presence of pores with diameters of around 100 μm in Fig. 4, it probably only detected the entry size of spherical pores. This is in agreement with SEM observations, where the maximum amount of spherical pores was evident in pure FS and FA AAMs, which had the largest amount of pores 1–2 μm in diameter in Fig. 4. Despite the similar porosity stated in Table 4, the 30 ma% FA containing AAM the later had higher compressive strengths than the pure FS AAM. This can probably be attributed to a better dissolution of the FA in 10 M NaOH, see Table 3, as well as to an elevated average amorphous content after the FA addition, see Supplement 3. The 30 ma% FA containing AAM almost showed no cracks in contrast to the 30 ma% LS AAM which contained very few spherical pores, while the ASN contained many cracks, see Supplements 6 g-I and 7 c, which probably caused the low compressive strength discernible in Fig. 1 although the amorphous content was even higher than in the FA containing AAMs.

The elemental composition in AAMs containing pure FS, 30 ma% of FA or 30 ma% of LS were analyzed using EDXS spot measurements at 49–59 locations/sample visually estimated to be the activated gel (Supplement 8), resulting element ratios are presented in Supplement 9 a-b.

Atomic% of Na, Mg, Al, Si and Ca (values available in Supplement 9 c) were analyzed using descriptive statistics. EDXS quantification in low vacuum mode without a standard is comparably unreliable which is why only a qualitative interpretation of selected element ratios is presented to determine statistical trends. The Si/Al ratio shows a unimodal distribution for pure FS and 30 ma% FA AAMs, while the 30 ma% LS AAM seems to have three modes. A high Si/Al ratio confirms a successful polymerization and points towards units connected by silicate links (Abdullah et al., 2018). Increased Si/Al ratios in AAMs generally result in higher compressive strengths due to the increased amount of Si-O-Si bonds (He et al., 2016). However, the highest Si/Al ratio in Supplement 9 a was observed in the 30 ma% LS sample affected by extensive shrinkage cracks which degrade the mechanical properties as shown in Fig. 1. The 30 ma% LS sample shows an increased Ca/Si ratio in Supplement 9 b, compared to the pure FS and 30 ma% FA AAM samples, which might indicate a coexistence of CSH and AAM gels (Yip et al., 2005). The presence of a CSH gel in AAMs has been reported to improve the compressive strength of such binders (Yip et al., 2005), but an effect was probably blurred by the formation of curing cracks in the samples analyzed here.

3.3. Alkali activation of calcined sediments with a K-based activator and performance improvement by adding FA or LS

Similarly to the Na-activated AAMs, mixtures with K-activators were also prepared. The bending and compressive strengths as well as the geometrical densities of the K-activator based AAMs prepared from the batches stated in Table 1 are presented in Fig. 5, the corresponding values are provided as Supplement 5. The AAMs based on the FS generally showed higher strengths and comparable or lower densities than those based on the AS, which contain a slightly higher amount of SiO₂, see, Table 2. K-activated AS reached 15.8 MPa, while FS 21.9 MPa. Adding FA or LS lead to an increase of the mechanical properties to respectively 31.1 or 27.1 MPa for FS and to 28.0 or 30.5 MPa for AS.

XRD-patterns acquired from pure FS-AAMs and those with 30 ma% additions of FA or LS mixed using the K-activator are presented in Fig. 6, the highest intensity reflections of selected phases identified during subsequent evaluation are highlighted. Similarly to the XRD results for Na-activated mixtures, the same mineral phases were identified and the reflection at $2\theta \approx 32.3^\circ$ corresponds to K-salts (kalcinite), again resulting from efflorescence, which is common in AA systems with high contents of alkaline activators (Xiao et al., 2020).

A detailed Rietveld refinement was performed on XRD-patterns acquired from powders of the respective AAMs. The main crystalline components of prepared AAMs are quartz, illite/muscovite and feldspar. Calcite and dolomite respectively occur in amounts below 1.7 and 6.5 ma%. 2.5 ma% ankerite was detected only in a K-activated AAM containing 30 ma% LS. The amorphous content in the K-activator AAMs ranges from 41 to 49 ma% and is hence always higher than that of the main precursor FS (38 ma%). The amorphous content in K-activated AAMs containing FA remained constant but increasing the amount of added FA resulted in a small increase of the compressive strength. The compressive strength increased similarly, although the amorphous content in K-activated AAMs containing LS slightly decreased when increasing the amount of added LS. The complete XRD results are stated in Supplement 3.

FTIR spectra of cured AAMs and the respectively used precursors are shown in Fig. 7. Similarly to the Na-activated AAMs, all AAMs contained water (minima between 1100 cm⁻¹ and 1200 cm⁻¹ and between 1645

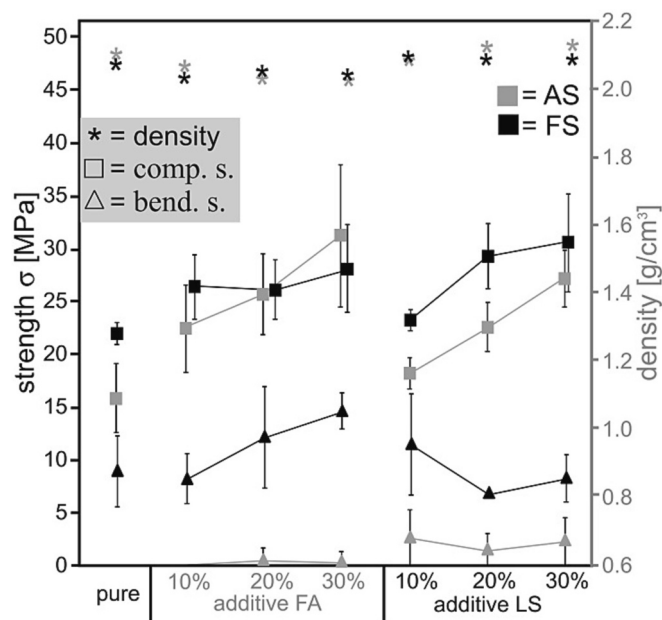


Fig. 5. Compressive and bending strengths of the K-activator based AAMs as well as their geometrical density, measured after curing for three days. Abbreviations: AS - calcined aged sediment, FS - calcined fresh sediment, FA - fly ash, LS - ladle slag.

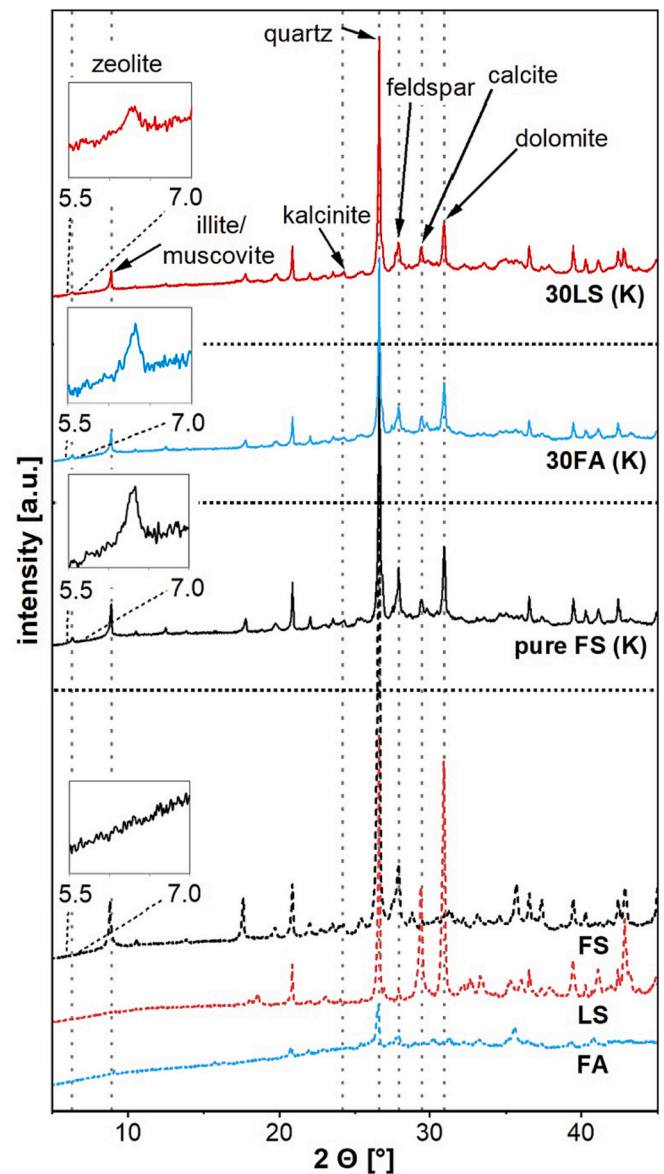


Fig. 6. XRD patterns of powdered precursors and FS-AAMs prepared using the pure sediment or containing 30 ma% FA or LS and activated using K-based solutions. The highest intensity reflections of subsequently identified phases are highlighted. The frames highlight the area around 6°. Abbreviations: FS - calcined fresh sediment, FA - fly ash, LS - ladle slag.

cm⁻¹ and 1652 cm⁻¹) as well as low quartz from the precursors (minima between 795 cm⁻¹ and 798 cm⁻¹). Similarly to Na-activated batches, a peak indicating Si-O-T asymmetric vibrations with minima between 964 cm⁻¹ and 979 cm⁻¹, i.e. shifted to lower wavenumbers than the same peaks in the precursors (988 cm⁻¹ and 992 cm⁻¹), implies that the Si/Al ratio in the ASN increased in favor of Si (Hajimohammadi et al., 2010).

MIP was performed on selected samples and the results are presented in Fig. 8 and Table 5.

The pores in all K-activated AAMs were unimodal distributed. Adding FA or LS shifted the median diameter towards higher values; from 0.40 for FS to 0.74 and 0.84 with the respective addition of FA or LS. In both cases, the overall porosity also increased (from 11.56 to 15.32 or 16.05). In contrast to the Na-activated AAMs featured in Fig. 4, no pores are detected in the range from 0.002 to the 0.02 μm. Pores with diameters between 0.02 and 0.1 μm most probably indicate a gel porosity (Chen et al., 2022).

Additionally, SEM analysis presented in the Supplements 10, 11 and

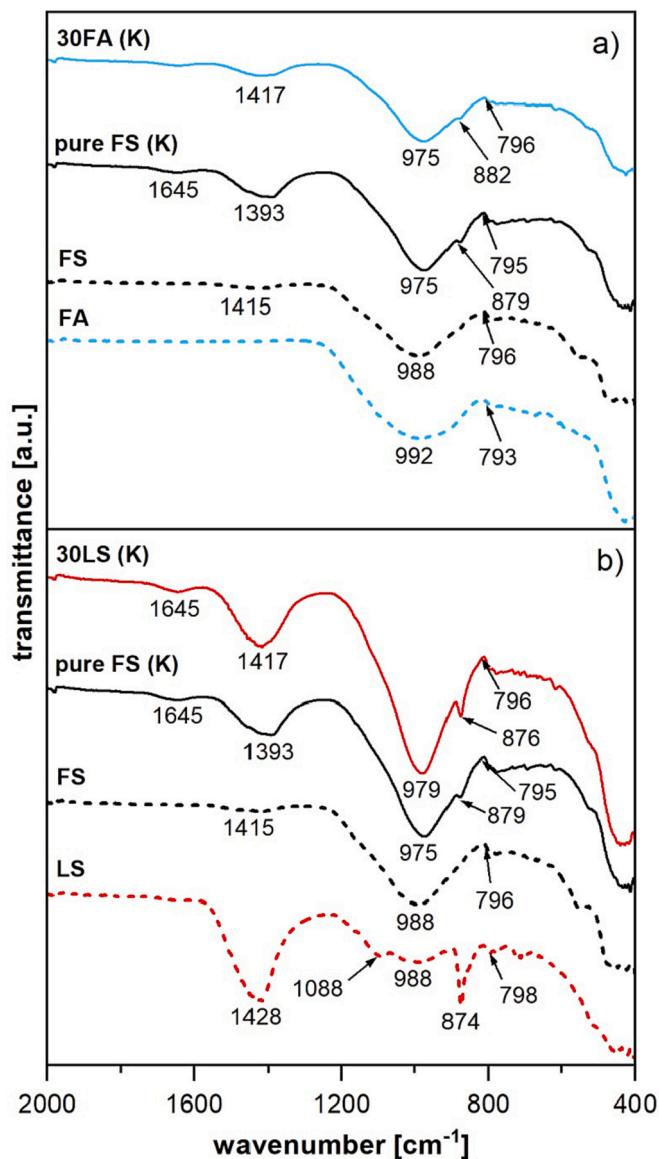


Fig. 7. FTIR spectra of the powdered precursors and FS-AAMs prepared using the pure sediment or containing 30 ma% a) FA or b) LS and activated using K-based solutions. Abbreviations: FS - calcined fresh sediment, FA - fly ash, LS - ladle slag.

12 revealed the presence of spherical macro pores (diameters from 10 to around 100 μm) caused by trapped gas and drying shrinkage induced cracks (width about 0.5 μm), see Fig. 8. Spherical pores were most common in 30 ma% FA containing AAM, Supplements 10 d-f and 11 b. Cracks were found in 30 ma% LS AAM, but in a very limited extent, see Supplement 10 g-i and 11 c, which was supported by low porosity values in Table 5. Again, MIP did not confirm presence of pores with diameters around 100 μm indicated in Fig. 8 and we assume that MIP only detected the entry size of spherical pores. This is in agreement with SEM observations, where the maximum amount of spherical pores was evident in 30 ma% FA AAM (Supplement 10), which had the largest amount of pores with diameters around 0.5 μm , see Fig. 8. Again the porosity did not have a negative influence on the compressive strengths.

Elemental compositions were investigated by EDXS spot measurements acquired at 42–55 locations/sample visually estimated to be composed of ASN gel (Supplement 12), selected element ratios are presented in Supplement 13.

Atomic% of K, Mg, Al, Si and Ca (values available in Supplement 13

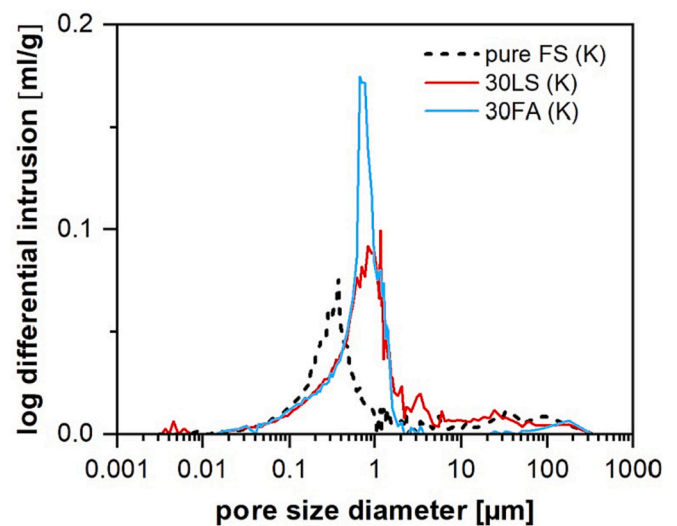


Fig. 8. Log differential intrusion vs. pore size of the powdered precursors and FS-AAMs prepared using the pure sediment or containing 30 ma% FA or LS and activated using K-based solutions. Abbreviations: FS - calcined fresh sediment, FA - fly ash, LS - ladle slag.

c) were analyzed by using descriptive statistics under the considerations outlined above. The frequency distribution diagram modes of the Si/Al atomic ratio show a trimodal distribution for pure FS and bimodal distributions for 30 ma% FA and LS AAMs in Supplement 13 a, indicating a disordered framework structure of AAMs caused by incorporation of K (Duxson et al., 2005). The highest Si/Al atomic ratio was observed in the pure FS sample. An increase of the Ca/Si atomic ratio is observed in the 30 ma% LS sample compared to pure FS and 30 ma% FA AAM samples in Supplement 13 b, most probably indicating the presence of a CSH gel which can improve the mechanical properties of Ca-rich alkali activated slag mortars (Zheng et al., 2021).

In summary, the results presented above show that the calcined sediments are suitable precursors for AAM materials if sufficient mechanical strengths are achieved. Adding co-binders like FA or LS enhances the mechanical strengths, especially in the case of FA due to its high amorphous content. In the case of LS the strength increase may be related to a simultaneous formation of AAM and CSH gels because of the increased Ca/Si atomic ratio and the increased amorphous content of LS-AAMs.

4. Conclusions

Two types of clay-rich river sediments accumulated at hydropower plant dams were analyzed as potential precursors for AAMs: fresh and aged sediment, the latter deposited for 10 years. Calcination increased the reactivity of both sediments. AAMs based on fresh sediments showed higher mechanical strengths than those based on aged sediments. Both Na- and K-based activators are suitable for the activation process and result in comparable mechanical properties. Adding FA or LS generally improved the mechanical properties of the resulting AAMs by about 50%. The compressive strength increase can be correlated to an increased amorphous content and increased solubility in alkaline media.

The calcined sediments can be used as the sole precursor in AAMs, but co-binders can enhance the mechanical properties. This study establishes an experimental procedure that may contribute to new strategies for the management of deposits accumulating at hydropower plant dams worldwide. Further analysis on the durability of this sediment based AAMs will be needed to be evaluating their long term application in the building sector.

Table 5

Results of the MIP analysis for K-activated samples. Abbreviations: FS - calcined fresh sediment, FA – fly ash, LS – ladle slag.

sample	FS [ma%]	porosity [%]	average pore diameter [μm]	median pore diameter [μm]	bulk density [g/mL]	skeletal density [g/mL]
pure FS (K)	–	11.56	0.22	0.40	2.20	2.48
FS-30FA (K)	30	15.32	0.34	0.74	2.08	2.46
FS-30LS (K)	30	16.05	0.22	0.84	2.16	2.57

Funding

This research was funded by the Slovenian Research Agency (ARRS) via project L7–2629: “Evaluation and remediation of sediments for further use in building sector (READY4USE)” and the research programme P2–0273 “Building structures and materials”.

CRedit authorship contribution statement

Lea Žibret: Formal analysis, Writing – original draft. **Wolfgang Wisniewski:** Writing – original draft, Writing – review & editing, Supervision. **Barbara Horvat:** Formal analysis, Writing – original draft. **Mojca Božič:** Conceptualization, Writing – review & editing, Funding acquisition. **Boštjan Gregorc:** Conceptualization, Funding acquisition. **Vilma Ducman:** Conceptualization, Methodology, Writing – review & editing, Supervision, Funding acquisition.

Declaration of Competing Interest

“The authors declare no conflict of interest.”

Data availability

All final data can be provided by authors.

Acknowledgments

We thank our colleagues at the ZAG Laboratory for Cements, Mortars and Ceramics for their technical support. The Metrology Institute of the Republic of Slovenia is acknowledged for the use of XRF.

Appendix A. Supplementary data

Supplementary data to this article can be found online at <https://doi.org/10.1016/j.clay.2023.106848>.

References

- Abdullah, M.M.A.B., Ming, L.Y., Yong, H.C., Tahir, M.F.M., 2018. Clay-based materials in geopolymer technology. In: Saleh, H.E.-D.M., Rahman, R.O.A. (Eds.), *Cement Based Materials*. InTech. <https://doi.org/10.5772/intechopen.74438>.
- Bernal, S.A., Rodríguez, E.D., Kirchheim, A.P., Provis, J.L., 2016. Management and valorisation of wastes through use in producing alkali-activated cement materials: Wastes producing alkali-activated cement materials. *J. Chem. Technol. Biotechnol.* 91, 2365–2388. <https://doi.org/10.1002/jctb.4927>.
- Bigozzi, M.C., Manzi, S., Lancellotti, I., Kamseu, E., Barbieri, L., Leonelli, C., 2013. Mix-design and characterization of alkali activated materials based on metakaolin and ladle slag. *Appl. Clay Sci.* 73, 78–85. <https://doi.org/10.1016/j.clay.2012.09.015>.
- Boldrini, G., Sgarlata, C., Lancellotti, I., Barbieri, L., Giorgetti, M., Ciabocco, M., Zamponi, S., Berrettoni, M., Leonelli, C., 2021. Efficient chemical stabilization of tannery wastewater pollutants in a single step process: Geopolymerization. *Sustain. Environ. Res.* 31, 33. <https://doi.org/10.1186/s42834-021-00106-7>.
- Češnovar, M., Traven, K., Horvat, B., Ducman, V., 2019. The potential of ladle slag and electric arc furnace slag use in synthesizing alkali activated materials; the influence of curing on mechanical properties. *Materials* 12, 1173. <https://doi.org/10.3390/ma12071173>.
- Chen, S., Ruan, S., Zeng, Q., Liu, Y., Zhang, M., Tian, Y., Yan, D., 2022. Pore structure of geopolymer materials and its correlations to engineering properties: a review. *Constr. Build. Mater.* 328, 127064 <https://doi.org/10.1016/j.conbuildmat.2022.127064>.
- Davidovits, J., 2017. Geopolymers: ceramic-like inorganic polymers. *J. Ceram. Sci. Technol.* <https://doi.org/10.4416/JCST2017-00038>.
- D'Elia, A., Pinto, D., Eramo, G., Giannossa, L.C., Venturi, G., Laviano, R., 2018. Effects of processing on the mineralogy and solubility of carbonate-rich clays for alkaline activation purpose: mechanical, thermal activation in red/ox atmosphere and their combination. *Appl. Clay Sci.* 152, 9–21. <https://doi.org/10.1016/j.clay.2017.11.036>.
- D'Elia, A., Pinto, D., Eramo, G., Laviano, R., Palomo, A., Fernández-Jiménez, A., 2020. Effect of alkali concentration on the activation of carbonate-high illite clay. *Appl. Clay Sci.* 10, 2203. <https://doi.org/10.3390/app10072203>.
- Ducman, V., Bizjak, K.F., Likar, B., Kolar, M., Robba, A., Imperl, J., Božič, M., Gregorc, B., 2022. Evaluation of sediments from the River Drava and their potential for further use in the building sector. *Materials* 15, 4303. <https://doi.org/10.3390/ma15124303>.
- Dupuy, C., Gharzouni, A., Texier-Mandoki, N., Bourbon, X., Rossignol, S., 2018. Thermal resistance of argillite-based alkali-activated materials. Part 1: effect of calcination processes and alkali cation. *Mater. Chem. Phys.* 217, 323–333. <https://doi.org/10.1016/j.matchemphys.2018.06.079>.
- Duxson, P., Lukey, G.C., Separovic, F., van Deventer, J.S.J., 2005. Effect of alkali Cations on aluminum incorporation in geopolymeric gels. *Ind. Eng. Chem. Res.* 44, 832–839. <https://doi.org/10.1021/ie0494216>.
- El-Habaak, G., Askalany, M., Abdel-Hakeem, M., 2018. The effect of mineralogy of calcined shales on the alkali activation and geopolymerization reactions: a case study from Abu-Tartur plateau, Western Desert. *Egypt. Appl. Clay Sci.* 162, 90–100. <https://doi.org/10.1016/j.clay.2018.05.025>.
- Ferone, C., Liguori, B., Capasso, I., Colangelo, F., Cioffi, R., Cappelletto, E., Di Maggio, R., 2015. Thermally treated clay sediments as geopolymer source material. *Appl. Clay Sci.* 107, 195–204. <https://doi.org/10.1016/j.clay.2015.01.027>.
- Gao, X., Yu, Q.L., Brouwers, H.J.H., 2015. Reaction kinetics, gel character and strength of Ambient temperature cured alkali activated slag–fly ash blends. *Constr. Build. Mater.* 11.
- Guo, X., Hu, W., Shi, H., 2014. Microstructure and self-solidification/stabilization (S/S) of heavy metals of nano-modified CFA–MSWIFA composite geopolymers. *Constr. Build. Mater.* 56, 81–86. <https://doi.org/10.1016/j.conbuildmat.2014.01.062>.
- Hajimohammadi, A., Provis, J.L., van Deventer, J.S.J., 2010. Effect of alumina release rate on the mechanism of geopolymer gel formation. *Chem. Mater.* 22, 5199–5208. <https://doi.org/10.1021/cm101151n>.
- Hájková, P., 2018. Kaolinite claystone-based geopolymer materials: effect of chemical composition and curing conditions. *Minerals* 8, 444. <https://doi.org/10.3390/min8100444>.
- He, P., Wang, M., Fu, S., Jia, D., Yan, S., Yuan, J., Xu, J., Wang, P., Zhou, Y., 2016. Effects of Si/Al ratio on the structure and properties of metakaolin based geopolymer. *Ceram. Int.* 42, 14416–14422. <https://doi.org/10.1016/j.ceramint.2016.06.033>.
- Horvat, B., Češnovar, M., Traven, K., Pavlin, M., König, K., Ducman, V., 2022. Influence of homogenization of alkali-activated slurry on mechanical strength. In: 3rd International Conference on Technologies & Business Models for Circular Economy: Conference Proceedings. Presented at the International Conference on Technologies & Business Models for Circular Economy. University of Maribor Press, pp. 11–50. <https://doi.org/10.18690/um.fkkt.2.2022.2>.
- Huseien, G.F., Sam, A.R.M., Shah, K.W., Mirza, J., Tahir, M.M., 2019. Evaluation of alkali-activated mortars containing high volume waste ceramic powder and fly ash replacing GBFS. *Constr. Build. Mater.* 210, 78–92. <https://doi.org/10.1016/j.conbuildmat.2019.03.194>.
- Kendall, K., Howard, A.J., Birchall, J.D., 1983. The relation between porosity, microstructure and strength, and the approach to advanced cement-based materials. *Philos. Trans. Roy. Soc. Lond. SA310*, 1511, 139–153. <https://doi.org/10.1098/rsta.1983.0073>.
- Khale, D., Chaudhary, R., 2007. Mechanism of geopolymerization and factors influencing its development: a review. *J. Mater. Sci.* 42, 729–746. <https://doi.org/10.1007/s10853-006-0401-4>.
- Khalifa, A.Z., Cizer, Ö., Pontikes, Y., Heath, A., Patureau, P., Bernal, S.A., Marsh, A.T.M., 2020. Advances in alkali-activation of clay minerals. *Cem. Concr. Res.* 132, 106050 <https://doi.org/10.1016/j.cemconres.2020.106050>.
- Khater, H.M., Abd el Gawaad, H.A., 2016. Characterization of alkali activated geopolymer mortar doped with MWNT. *Constr. Build. Mater.* 102, 329–337. <https://doi.org/10.1016/j.conbuildmat.2015.10.121>.
- Komnitsas, K., Zaharaki, D., Vlachou, A., Bartzas, G., Galetakis, M., 2015. Effect of synthesis parameters on the quality of construction and demolition wastes (CDW) geopolymers. *Adv. Powder Technol.* 26, 368–376. <https://doi.org/10.1016/j.apt.2014.11.012>.
- Koutník, P., Soukup, A., Bezucha, P., Šafář, J., Kohout, J., 2020. Low viscosity metakaolinite based geopolymer binders. *Constr. Build. Mater.* 230, 116978 <https://doi.org/10.1016/j.conbuildmat.2019.116978>.
- Kuenzel, C., Vandepierre, L.J., Donatello, S., Boccaccini, A.R., Cheeseman, C., 2012. Ambient Temperature Drying Shrinkage and cracking in Metakaolin-based Geopolymers. *J. Am. Ceram. Soc.* 95, 3270–3277. <https://doi.org/10.1111/j.1551-2916.2012.05380.x>.
- Kumar, A., Kumar, S., 2013. Development of paving blocks from synergistic use of red mud and fly ash using geopolymerization. *Constr. Build. Mater.* 38, 865–871. <https://doi.org/10.1016/j.conbuildmat.2012.09.013>.

- Lee, S., Jou, H.-T., van Riessen, A., Rickard, W.D.A., Chon, C.-M., Kang, N.-H., 2014. Three-dimensional quantification of pore structure in coal ash-based geopolymer using conventional electron tomography. *Constr. Build. Mater.* 52, 221–226. <https://doi.org/10.1016/j.conbuildmat.2013.10.072>.
- Lucas, S., Tognonvi, M.T., Gelet, J.-L., Soro, J., Rossignol, S., 2011. Interactions between silica sand and sodium silicate solution during consolidation process. *J. Non-Cryst. Solids* 357, 1310–1318. <https://doi.org/10.1016/j.jnoncrysol.2010.12.016>.
- Mabroum, S., Aboulayt, A., Taha, Y., Benzazaoua, M., Semlal, N., Hakkou, R., 2020. Elaboration of geopolymers based on clays by-products from phosphate mines for construction applications. *J. Clean. Prod.* 261, 121317. <https://doi.org/10.1016/j.jclepro.2020.121317>.
- Madsen, I.C., Scarlett, N.V.Y., Kern, A., 2011. Description and survey of methodologies for the determination of amorphous content via X-ray powder diffraction. *Z. Für. Krist.* 226, 944–955. <https://doi.org/10.1524/zkri.2011.1437>.
- Marsh, A., Heath, A., Patureau, P., Evernden, M., Walker, P., 2018. Alkali activation behaviour of un-calcined montmorillonite and illite clay minerals. *Appl. Clay Sci.* 166, 250–261. <https://doi.org/10.1016/j.clay.2018.09.011>.
- McLellan, B.C., Williams, R.P., Lay, J., van Riessen, A., Corder, G.D., 2011. Costs and carbon emissions for geopolymer pastes in comparison to ordinary Portland cement. *J. Clean. Prod.* 19, 1080–1090. <https://doi.org/10.1016/j.jclepro.2011.02.010>.
- Messina, F., Ferone, C., Molino, A., Roviello, G., Colangelo, F., Molino, B., Cioffi, R., 2017. Synergistic recycling of calcined clayey sediments and water potabilization sludge as geopolymer precursors: Upscaling from binders to precast paving cement-free bricks. *Constr. Build. Mater.* 133, 14–26. <https://doi.org/10.1016/j.conbuildmat.2016.12.039>.
- Mostefa, F., Bouhamou, N.E., Mesbah, H.A., Aggoun, S., Mekhatria, D., 2018. Sedimentary clays as geopolymer precursor. *Int. J. Eng. Res. Afr.* 39, 97–111. <https://doi.org/10.4028/www.scientific.net/JERA.39.97>.
- Nawaz, M., Heitor, A., Sivakumar, M., 2020. Geopolymers in construction - recent developments. *Constr. Build. Mater.* 260, 120472. <https://doi.org/10.1016/j.conbuildmat.2020.120472>.
- Nouri, A., Sola, A., 2018. Metal particle shape: a practical perspective. *Met. Powder Rep.* 73, 276–282. <https://doi.org/10.1016/j.mprp.2018.04.001>.
- Obenaus-Emler, R., Falah, M., Illikainen, M., 2020. Assessment of mine tailings as precursors for alkali-activated materials for on-site applications. *Constr. Build. Mater.* 246, 118470. <https://doi.org/10.1016/j.conbuildmat.2020.118470>.
- Panagiotopoulou, Ch., Kontori, E., Perraki, Th., Kakali, G., 2007. Dissolution of aluminosilicate minerals and by-products in alkaline media. *J. Mater. Sci.* 42, 2967–2973. <https://doi.org/10.1007/s10853-006-0531-8>.
- Pavlin, M., Horvat, B., Ducman, V., 2022. Preparation of façade panels based on alkali-activated waste mineral wool, their characterization, and durability aspects. *Int. J. Appl. Ceram. Technol.* 19, 1227–1234. <https://doi.org/10.1111/ijac.13998>.
- Promentilla, M.A.B., Sugiyama, T., Hitomi, T., Takeda, N., 2009. Quantification of tortuosity in hardened cement pastes using synchrotron-based X-ray computed microtomography. *Cem. Concr. Res.* 39, 548–557. <https://doi.org/10.1016/j.cemconres.2009.03.005>.
- Provis, J.L., 2018. Alkali-activated materials. *Cem. Concr. Res.* 114, 40–48. <https://doi.org/10.1016/j.cemconres.2017.02.009>.
- Provis, J.L., Lukey, G.C., van Deventer, J.S.J., 2005. Do geopolymers actually contain nanocrystalline zeolites? A reexamination of existing results. *Chem. Mater.* 17, 3075–3085. <https://doi.org/10.1021/cm050230i>.
- Provis, J.L., Myers, R.J., White, C.E., Rose, V., van Deventer, J.S.J., 2012. X-ray microtomography shows pore structure and tortuosity in alkali-activated binders. *Cem. Concr. Res.* 42, 855–864. <https://doi.org/10.1016/j.cemconres.2012.03.004>.
- Provis, J.L., Palomo, A., Shi, C., 2015. Advances in understanding alkali-activated materials. *Cem. Concr. Res.* 78, 110–125. <https://doi.org/10.1016/j.cemconres.2015.04.013>.
- Razak, R., Abdullah, M., Hussin, K., Ismail, K., Hardjito, D., Yahya, Z., 2015. Optimization of NaOH molarity, LUSI Mud/alkaline activator, and Na₂SiO₃/NaOH ratio to produce lightweight aggregate-based geopolymer. *Int. J. Mol. Sci.* 16, 11629–11647. <https://doi.org/10.3390/ijms160511629>.
- Rovnanik, P., Bayer, P., Rovnaniková, P., 2013. Characterization of alkali activated slag paste after exposure to high temperatures. *Constr. Build. Mater.* 47, 1479–1487. <https://doi.org/10.1016/j.conbuildmat.2013.06.070>.
- Sabbatini, A., Vidal, L., Pettinari, C., Sobrados, L., Rossignol, S., 2017. Control of shaping and thermal resistance of metakaolin-based geopolymers. *Mater. Des.* 116, 374–385. <https://doi.org/10.1016/j.matdes.2016.12.039>.
- Šajn, R., Halamić, J., Peh, Z., Galović, L., Alijagić, J., 2011. Assessment of the natural and anthropogenic sources of chemical elements in alluvial soils from the Drava River using multivariate statistical methods. *J. Geochem. Explor.* 110, 278–289. <https://doi.org/10.1016/j.gexplo.2011.06.009>.
- Sarkar, M., Dana, K., Das, S., 2015. Microstructural and phase evolution in metakaolin geopolymers with different activators and added aluminosilicate fillers. *J. Mol. Struct.* 1098, 110–118. <https://doi.org/10.1016/j.molstruc.2015.05.046>.
- Schmid, S.M., Scharf, A., Handy, M.R., Rosenberg, C.L., 2013. The Tauern Window (Eastern Alps, Austria): a new tectonic map, with cross-sections and a tectonometamorphic synthesis. *Swiss J. Geosci.* 106, 1–32. <https://doi.org/10.1007/s00015-013-0123-y>.
- Sgarlata, C., Formia, A., Siligardi, C., Ferrari, F., Leonelli, C., 2021. Mine clay washing residues as a source for alkali-activated binders. *Materials* 15, 83. <https://doi.org/10.3390/ma15010083>.
- SIST EN 1097-7, 2008. Tests for Mechanical and Physical Properties of Aggregates-Part 7: Determination of the Particle Density of Filler-Pyknometer Method.
- Škvára, F., 2007. Alkali activated material. *Geopolymer* 16.
- Šoster, A., Zavašnik, J., Ravnjak, M., Herlec, U., 2017. REE-bearing minerals in Drava river sediments, Slovenia, and their potential origin. *Geologija* 60, 257–266. <https://doi.org/10.5474/geologija.2017.018>.
- Thapa, V.B., Waldmann, D., Wagner, J.-F., Lecomte, A., 2018. Assessment of the suitability of gravel wash mud as raw material for the synthesis of an alkali-activated binder. *Appl. Clay Sci.* 161, 110–118. <https://doi.org/10.1016/j.clay.2018.04.025>.
- Traven, K., Češnovar, M., Škapin, S.D., Ducman, V., 2021. High temperature resistant fly-ash and metakaolin-based alkali-activated foams. *Ceram. Int.* 47, 25105–25120. <https://doi.org/10.1016/j.ceramint.2021.05.241>.
- Turner, L.K., Collins, F.G., 2013. Carbon dioxide equivalent (CO₂-e) emissions: a comparison between geopolymer and OPC cement concrete. *Constr. Build. Mater.* 43, 125–130. <https://doi.org/10.1016/j.conbuildmat.2013.01.023>.
- Werling, N., Kaltenbach, J., Weidler, P.G., Schuhmann, R., Dehn, F., Emmerich, K., 2022. Solubility of Calcined kaolinite, montmorillonite, and illite in high molar NaOH and suitability as precursors for geopolymers. *Clay Clay Miner.* 70, 270–289. <https://doi.org/10.1007/s42860-022-00185-6>.
- Wongsa, A., Boonserm, K., Waisurasingha, C., Sata, V., Chindaprasit, P., 2017. Use of municipal solid waste incinerator (MSWI) bottom ash in high calcium fly ash geopolymer matrix. *J. Clean. Prod.* 148, 49–59. <https://doi.org/10.1016/j.jclepro.2017.01.147>.
- Xiao, R., Ma, Y., Jiang, X., Zhang, M., Zhang, Y., Wang, Y., Huang, B., He, Q., 2020. Strength, microstructure, efflorescence behavior and environmental impacts of waste glass geopolymers cured at ambient temperature. *J. Clean. Prod.* 252, 119610. <https://doi.org/10.1016/j.jclepro.2019.119610>.
- Yan, S., Sagoe-Crentsil, K., 2012. Properties of wastepaper sludge in geopolymer mortars for masonry applications. *J. Environ. Manag.* 112, 27–32. <https://doi.org/10.1016/j.jenvman.2012.07.008>.
- Yip, C.K., Lukey, G.C., van Deventer, J.S.J., 2005. The coexistence of geopolymeric gel and calcium silicate hydrate at the early stage of alkaline activation. *Cem. Concr. Res.* 35, 1688–1697. <https://doi.org/10.1016/j.cemconres.2004.10.042>.
- Zheng, D., Ji, T., Wang, G., 2021. Effect of CaO on the Autogenous Shrinkage of alkali-activated slag mortar. *Adv. Mater. Sci. Eng.* 2021, 1–9. <https://doi.org/10.1155/2021/9918834>.